ADVANCED FUNCTIONAL MATERIALS
www.afm-journal.de

Solution-pH-Modulated Rectification of Ionic Current in Highly Ordered Nanochannel Arrays Patterned with Chemical Functional Groups at Designed Positions

*Cheng-Yong Li, Feng-Xiang Ma, Zeng-Qiang Wu, Hong-Li Gao, Wen-Ting Shao, Kang Wang, and Xing-Hua Xia**

A new ionic current rectification device responsive to a broad range of pH stimuli is established using highly ordered nanochannels of porous anodic alumina membrane with abrupt surface charge discontinuity. The asymmetric surface charge distribution is achieved by patterning the nanochannels with surface amine functional groups at designed positions using a two-step anodization process. Due to the protonation/deprotonation of the patterned amine and the remaining intrinsic hydroxyl groups upon solution pH variation, the nanochannel-array-based device is able to regulate ion transport selectivity and has ionic current rectification properties. The rectification ratio of the device is mainly determined by the nanochannel size, and the rectification ratio is less sensitive to the patterned length of the amine groups when the nanochannels size is defined. Thus, the isoelectric point of nanochannels can be easily estimated to be the pH value with a unit rectification ratio. The present ionic device is promising for biosensing, molecular transport and separation, and drug delivery in confined environments.

1. Introduction

The transport of mass and charge in nanoconfined spaces with at least one dimension smaller than 100 nm enables the occurrence of novel phenomena which are not observed in the bulk.[1] For example, the flow of water inside hydrophobic carbon nanotubes is much faster than in the bulk.[2] Ion mobility in nanoconfined spaces is also much higher than the bulk.[3] These phenomena demonstrate that the controlled transport of mass and charge through nanoconfined spaces is a fundamental process of interest in biology, physics and chemistry.[4] Recent results strongly suggest that as the nanochannel size becomes comparable to the thickness of electric double layer (EDL), novel ion transport properties similar to biological protein nanopores emerge, such as ion selectivity, ionic current rectification (ICR) and current fluctuation have been observed.[4f,5]

The ionic current rectification has been extensively studied using nanopore devices.[5c,5d,5f–h,5j–l,6] In ICR devices, the current at a voltage of one polarity is significantly larger or lower than the one at opposite voltage polarity, a characteristic behavior of semiconductor diodes. This phenomenon originates from the asymmetric distribution of potential across the nanopores and nanochannels.[5d] Much excellent work about ICR in conical nanopores has been reported since the first example of an artificial rectification nanopore system reported in 1997 using conical glass nanopipettes.[5c–f,5h,6b,7] The natural presence of intrinsic charge distribution in the conical nanopore due to the asymmetric geometry configuration makes it ready to achieve ICR. In the case of a nanochannel with relatively uniform diameter, the surface charge is usually distributed homogeneously. Achieving ICR is seldom reported. Single heterojunctions nanofluidic diodes with opposite surface charges on two segments of the channel walls were fabricated with the development of micro/nanofabrication technology. Yang et al. reported the rectification of single heterojunctions nanofluidic diodes composed with heterostructured Al_2O_3/SiO_2 nanotubes using atomic layer deposition (ALD), protection/deprotection, and selective etching.[8] Cheng et al. investigated several ion transport and rectification behaviors in sub-20 nm nanofluidic channels consisting of SiO_2 and Al_2O_3 heterogeneous oxide materials using photolithography, electron-beam evaporation (EBE), and lift off processes.[6g] Wu et al. prepared the heterostructured nanopore membranes composed of Al_2O_3 and SiO_2 layers with nanopore array for ionic current rectification using reactive ion etching (RIE) and a pattern transfer process.[6h] These works utilized distinct isoelectric points of two different oxide materials to form positively and negatively charged surface abrupt junction. However, they are not suitable for large scale application due to the complicated preparation processes and requirement of special equipment. Therefore, selective modification of the uniform nanochannels with functional groups should be an ideal strategy to obtain asymmetric surface charge distribution

C.-Y. Li, F.-X. Ma, Z.-Q. Wu, H.-L. Gao, W.-T. Shao, K. Wang, Prof. X.-H. Xia
State Key Laboratory of Analytical Chemistry for Life Science
School of Chemistry and Chemical Engineering
Nanjing University
Nanjing 210093, China
E-mail: xhxia@nju.edu.cn

DOI: 10.1002/adfm.201300315

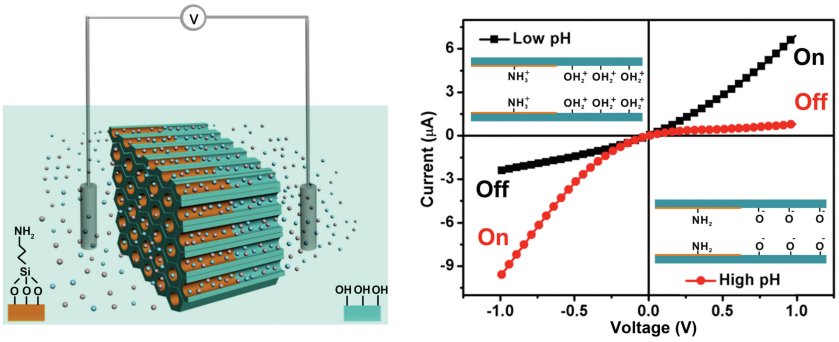

Figure 1. Schematic illustration of rectification characterization for PAA membrane patterned with APTMS.

for selectively regulating ions transport. An effective modification of nanochannel surface with chemical groups is called as diffusion-limited patterning (DLP).[9] In this approach, a functional molecule is placed only on one side of the membrane and diffuses along the nanochannel axis. The length and density of modified functional molecules rely on reagent concentration, the diffusion coefficient and time, the reagent reaction rate and the nanochannel geometry, therefore, they cannot be exactly controlled because of the many influential factors. In particular, the diffusion process is very complicated in nanoconfined spaces.[10] Meanwhile, the concentration of the reagent in the entering region is high and decays along the nanochannel axis.[5f] This would result in the quantity of charge density being reduced gradually along the nanochannel axis, which is not beneficial for high performance of ICR requiring sudden change of geometry or charge density.

Here, an ICR device responsive to a broad range of pH stimuli has been constructed using highly ordered nanochannels of a porous anodic alumina (PAA) membrane with abrupt surface charge discontinuity (as shown in **Figure 1**). The nanochannels with asymmetric surface charge discontinuity have small diameter and very high aspect ratio such that entering ions can be effectively confined and thus, novel charge transport properties could be expected. Patterning of the nanochannels with amine groups of 3-aminopropyltrimethoxy-silane (APTMS) is realized using a modified two-step anodization of aluminum in acidic media as reported previously.[11] For obtaining relatively well organized nanochannel array, a pre-anodization process is adopted. The surface property of nanochannels can be regulated easily by chemical modification method which is much simple and convenient compared with the ALD, EBE, and RIE methods.[8,6g,6h] Compared with the DLP method, the surface charge of nanochannels can be changed suddenly with the present modification method, and the patterned length of surface functional groups can be accurately defined at will by controlling the anodization time.[9] Using the two-step anodization process, nanochannels with diameter of 20 nm and 40 nm have been fabricated by using sulfuric acid and oxalic acid aqueous solutions, respectively.[12] Results show that the ionic current of the PAA membrane reaches the microampere level due to the extremely high pore density, which is several orders of magnitude larger than single nanopores, suited for building ion devices with less sensitive electronic detection equipments.[5e,13] On the other hand, preparation of a PAA membrane using a simple two-step anodization method is much easier and less expensive than fabrication of nanopore devices. Meanwhile, the mechanism of ICR in cylindrical nanochannels with asymmetric surface charge distribution was studied by using finite element method (FEM). Theoretical simulations show that ion accumulation and depletion caused by non-uniform surface charge distribution are the main reason for ICR. The present work demonstrates for the first time the integration of functional groups modification at designed positions in PAA membrane to achieve an ICR device responding to pH stimuli. We believe that the present ICR device may find potential applications in biosensing, molecular transport and separation, and drug delivery in confined environments.

2. Results and Discussion

2.1. Fabrication of PAA Membranes

Aluminum sheets were cleaned in acetone and then electrochemically polished with perchloric acid/ethanol (1:9 v/v $HClO_4$: EtOH) at a constant voltage of 10 V for 10 min to achieve a mirror-finished surface. The temperature of the electrolyte was maintained at 2 °C. The two-step fabrication approach is schematically shown in **Figure 2**. Before performing the two-step anodization process, a pre-anodization process is introduced to obtain relatively well organized nanochannels (procedures a,b). The formed concaves are used as the nucleation sites for the following classic anodization process. Upon completion of the first anodization (procedure c), PAA membrane is then hydroxylated in boiled hydrogen peroxide (30% H_2O_2) for 2 h and thoroughly dried under a stream of nitrogen gas. Subsequently, the membrane is treated with 10% of 3-aminopropyltrimethoxysilane solution diluted in acetone for 12 h (procedure d). After washing, the APTMS modified PAA membrane is cured in an oven at 120 °C for 2 h to crosslink the silane layer. The second anodization (procedure e) is then performed to generate an additional porous layer below the silanized porous one. The length of APTMS patterning and unmodified nanochannels can be controlled by the anodization step (c) and the anodization time of step (e), respectively. It is found that the silanized surfaces are chemically inert and mechanically stable under the anodization conditions. Finally, free-standing PAA membranes are formed by removing the remaining aluminum layer using $SnCl_2$ solution followed by a bottom pore opening step carried out by immersing in 5 wt% phosphoric acid.[12a]

PAA membranes of about 40 nm nanochannel diameter were prepared by anodic oxidation of pure aluminum sheets in a 0.3 M oxalic acid electrolyte at a constant voltage of 50 V at 20 °C. PAA membranes of about 20 nm nanochannel diameter were fabricated in a 0.2 M sulfuric acid at a constant voltage of 20 V

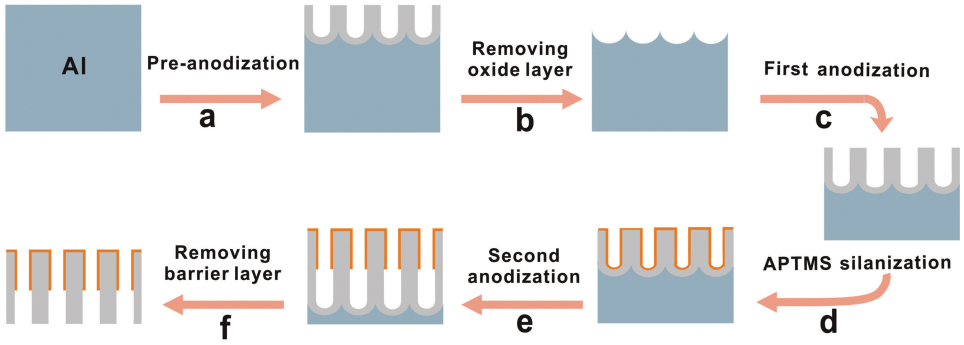

Figure 2. Schematic illustration of the method for fabricating PAA membrane with patterned APTMS.

at 10 °C. The thickness of PAA membranes can be adjusted by the anodization time.

2.2. Structure Characterizations of PAA Membranes

Figure 3A–D show the scanning electron microscopy (SEM) images of PAA membrane prepared at 50 V in 0.3 M oxalic acid solution. It can be estimated that the pore diameter of PAA membrane is about 40 nm (both top and bottom, as shown in Figure 3A,B). The thickness of the membrane is estimated to be 70 μm (Figure 3D). A regular cylinder nanochannel array parallel to each other is clearly shown (Figure 3C). There is no significant contrast between the two layers with surface functionality from the cross-sectional SEM images. Fluorescent probe fluorescein isothiocyanate (FITC) is therefore selectively bounded to the APTMS functional layer. A cross-sectional laser scanning confocal microscopy (LSCM) image (Figure 3E) of the bilayered membrane clearly shows a strong green florescence of the upper layer as compared to the lower layer. The thickness of the APTMS layer in the bilayered membrane is about 45 μm, which can be modulated with the anodization time (step c) (Figure 3E and Figure S5 in the Supporting Information).

The presence of APTMS in the PAA membrane was characterized using X-ray photoelectron spectroscopy (XPS) (**Figure 4**). The non-modified PAA membrane does not show the Si2P

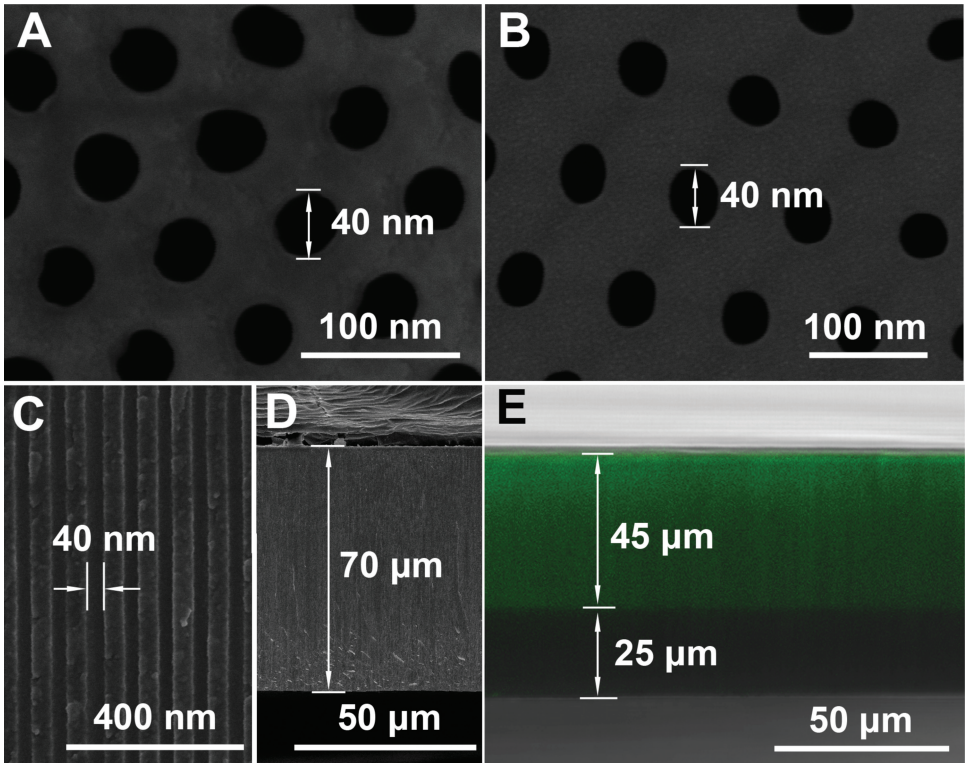

Figure 3. SEM (a: top; b: bottom; c: cross-section; d: the whole cross-section) and LSCM (e: the whole cross-section) images of the PAA membrane fabricated at 50 V in 0.3 M oxalic acid solution. The anodization times for steps (c) and (e) were 4 h and 2.5 h, respectively.

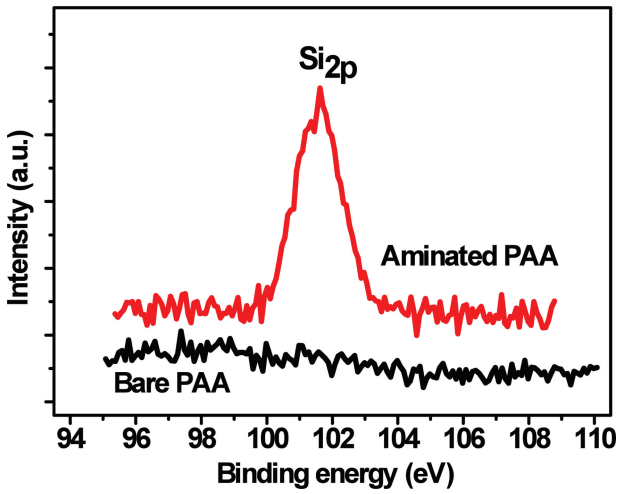

Figure 4. XPS spectra of the PAA membranes fabricated at 50 V in 0.3 M oxalic acid solution without (bare PAA) and with modification by APTMS. The anodization times for steps (c) and (e) were 4 h and 2.5 h, respectively.

peak. As the membrane is treated with APTMS, a clear peak of Si2P appears. These results are in accordance with the result in Figure 3E.

2.3. Rectification Characterizations of 40 nm PAA Membranes

Alumina is a kind of amphoteric material with surface charge properties that are determined by the solution pH.[14] When the pH is lower than its isoelectric point (pI), alumina will be protonated and its surface will carry positive charges (reaction (1)). In contrast, the alumina carries negative charges in solution pH above pI due to the deprotonation as reaction (2):

$$Al-OH+H^+ \rightarrow Al-OH_2^+ \quad \text{low pH (1)}$$

$$Al-OH+OH^- \rightarrow Al-O^- + H_2O \quad \text{high pH (2)}$$

The pKa of the siloxane-tethered monolayers of amines in nanochannels of PAA membranes has been studied and was found to be 6.2.[15] The surface -NH_2 groups on the interior pore surface are initially protonated at low pHs range (reaction (3)) and neutral at high pH.

$$-NH_2+H^+ \rightarrow -NH_3^+ \quad \text{low pH (3)}$$

Figure 5A,B shows the i-V curves recorded using 40 nm diameter nanochannel array of PAA membranes under symmetric electrolyte conditions for different pH values of 1 mM KCl (the Debye length $\lambda \approx 10$ nm[10a]) when the potential applied to the working electrode at the APTMS modified layer is positive. At high pH values, the intrinsic alumina is deprotonated and carries negative charges, while the amino group is neutral. The negatively charged nanochannels have excess counterions (K^+ and H^+) and will exclude coions (Cl^- and OH^-) relative to the bulk. Thus, the currents carried by K^+ and H^+ are much larger than Cl^- and OH^-. The nanochannels show the rectification characteristics as follows: a high conducting ("on") state for $V < 0$ and a low conducting ("off") state for $V > 0$ (Figure 5B). It should be noted that the polarity of the rectification effect is determined by the polarity of the surface charges. At low pH values, both the ionized amino groups (–NH_3^+) and unmodified protonated alumina (–OH_2^+) are positively charged. The charge polarities are the same as positive. However, the positive

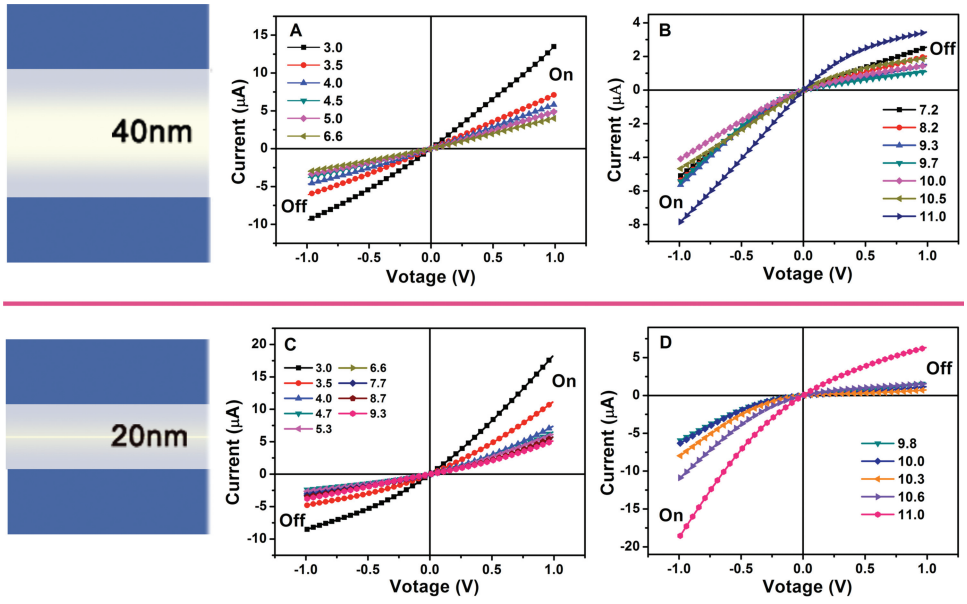

Figure 5. Experimental ionic rectification characteristic of PAA membranes measured in 1 mM KCl with different pH values. A,B) PAA membrane (diameter: 40 nm) was fabricated at 50 V in 0.3 M oxalic acid solution. The anodization times for steps (c) and (e) were 4 h and 2.5 h, respectively. C,D) PAA membrane (diameter: 20 nm) was fabricated at 20 V in 0.2 M sulfuric acid solution. Both the anodization times for steps (c) and (e) were 20 h.

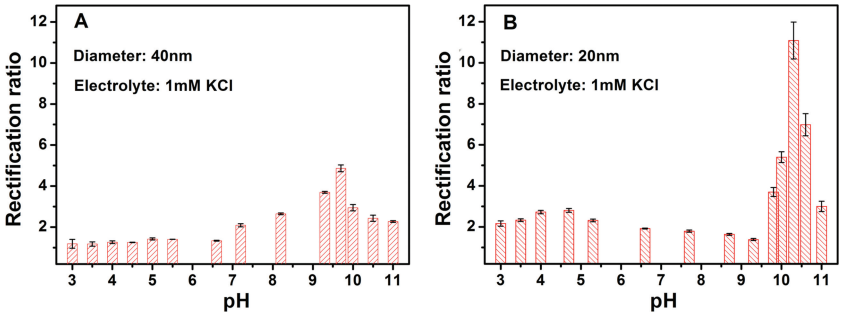

Figure 6. Ionic rectification ratio of PAA membranes measured in 1 mM KCl with different pH values. A) PAA membrane (diameter: 40 nm) was fabricated at 50 V in 0.3 M oxalic acid solution. B) PAA membrane (diameter: 20 nm) was fabricated at 20 V in 0.2 M sulfuric acid solution. Errors bars are ±σ for $n = 3$.

charge density is different along the nanochannels axis. The unmodified surface has more positive charges than the portion modified with APTMS because of the three Si-O bonded with three Al-OH, generating only one amino ($-NH_2$) group. Thus, the positive charge density in APTMS modification nanochannels is reduced. In this case, occurrence of ICR is due to the inhomogeneous distribution of the positive charges in the nanochannels. The nanochannels show the reversed rectification properties: a high conducting ("on") state for $V > 0$ and a low conducting ("off") state for $V < 0$ (Figure 5A). The transition between these two rectification regimes occurs at pH = 6.6, which is close to the pI (6.5) of PAA membranes fabricated in oxalic acid.[14] When the solution pH approaches to the pI of PAA, the i-V curve shows a linear, Ohmic behavior.

Rectification can be represented quantitatively as the ICR ratio, *r*, defined as the ratio between currents measured at voltages of the same amplitude but opposite polarity. In our case, *r* is defined as the absolute value of the current ratio *I* (on state)/*I* (off state), measured at ±1 V applied potential.

$$r = \frac{|I_{on}|}{|I_{off}|} \quad (4)$$

As shown by the i-V curves, the rectification characteristics are obviously different for nanochannels in 1 mM KCl solution with different pH. It is found that the ICR ratio changes between 1 and 2 in acidic KCl solutions and reaches maximum value of 4.8 at pH = 9.7 (**Figure 6**A). As mentioned previously, surface charges distribution is more asymmetric in alkaline solutions than in acidic solutions. The rectification ratio increases as the asymmetric charge distribution becomes more obvious. At first, the ICR ratio increases as pH value increases from 7 to 10 and reaches a maximum value. Then, it decreases when pH increases further in alkaline solutions. This decrease phenomenon could be due to the partially dissolution of amino groups due to the slow dissolution of alumina in strong basic solutions. Meanwhile, at higher concentration of solutions, the effect of surface charges is smaller due to high bulk ionic concentration since EDL thickness decreases with increasing the electrolyte concentration. This is not beneficial for enhancing ICR ratio. These results reveal that the ICR ratio can be modulated easily and the rectification polarity can be reversed by simply changing the solution pH values. Therefore, PAA membranes show tunable ionic selectivity and rectification characteristics.

In order to confirm the selectivity of the membranes, ions transport experiments were carried out. The fluorescent probe $Ru(bpy)_3Cl_2$ was selected because its fluorescence intensity will not be changed by solution pH. In addition, $Ru(bpy)_3Cl_2$ cannot specifically adsorb to amino group of PAA membrane modified with APTMS. **Figure 7** shows the distinct diffusion behavior of $Ru(bpy)_3^{2+}$ through 40 nm PAA membrane modified with APTMS in 1 mM KCl solution at different pH values. The $Ru(bpy)_3Cl_2$ concentration is obtained by analyzing the curves of fluorescence spectra versus time (Supporting Information Figure S8) and fluorescence standard curve (Supporting Information Figure S9). The slopes of straight-line plots of concentration versus time provide the diffusion flux of $Ru(bpy)_3^{2+}$ across the membrane. The $Ru(bpy)_3^{2+}$ diffusion flux is calculated as 9.74×10^{-7} mol m^{-2} s^{-1} in neutral solution. When the solution pH value is increased to 10.0, the $Ru(bpy)_3^{2+}$ diffusion flux reaches 1.75×10^{-6} mol m^{-2} s^{-1}. However, the $Ru(bpy)_3^{2+}$ diffusion flux decreases to 5.28×10^{-7} mol m^{-2} s^{-1} when the solution pH value is changed to 4.0. Lower diffusion flux is observed at lower pH values. This difference can be explained by the electrostatic interactions in nanochannels. When the solution pH value is above the pI of the PAA membrane, there is strong electrostatic attraction between $Ru(bpy)_3^{2+}$ and Al-O^- on the surface of nanochannels, resulting in a maximum flux since $Ru(bpy)_3^{2+}$ can diffuse through the nanochannels easily. At pH values below the pI, the diffusion flux decreases due to the electrostatic repulsion between $Ru(bpy)_3^{2+}$ and Al-OH_2^+ on the surface of nanochannels.

2.4. Rectification Characterizations of 20 nm PAA Membranes

Considering that the rectification ratio is highly dependent on the size of nanochannels, i-V curves were measured using

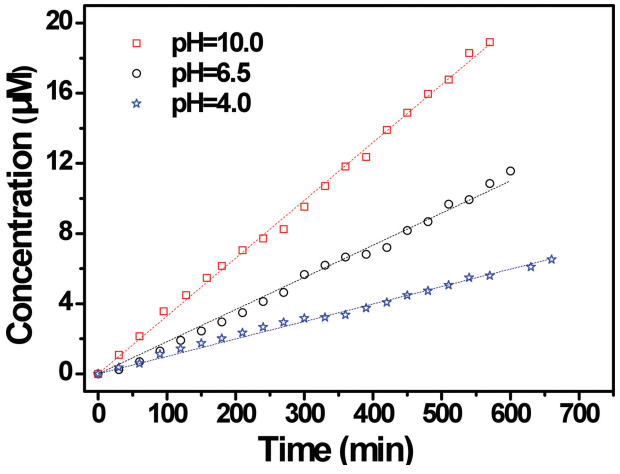

Figure 7. Concentration of $Ru(bpy)_3Cl_2$ transported across the nanochannels versus time in different pH solution.

20 nm diameter nanochannel array of PAA membranes in 1 mM KCl solutions with various pH values. It has been reported that the PAA membranes prepared in sulfuric acid usually have the smaller pore sizes.[16] In our experiments, the pore diameter of both the top and bottom surfaces is about 20 nm (Supporting Information Figure S2A–C). The thickness of the membrane is estimated to be 85 μm (Supporting Information Figure S2D), and the APTMS layer in the bilayered membrane is about 45 μm (Supporting Information Figure S2E).

The rectification characteristics of the 20 nm PAA membranes are shown in Figure 5C,D. The i-V curves display a better rectification behavior than 40 nm PAA membranes. As can been seen from Figure 6B, the rectification ratio is obviously higher than 40 nm PAA membranes under the same conditions (Figure 6A). In terms of *r*, the pH variation enhances a change of rectification efficiency from 2 to 12. This could be due to obvious overlap of the EDL in 20 nm nanochannels since the EDL thickness is about 10 nm in 1 mM KCl.[10a] The role of EDL in regulating ions transport is weakened in 40 nm PAA membranes resulting in increased free transport region in nanochannels.[5i,5o,10a,15] In addition, the polarity of ICR is reversed between pH = 9.3 and pH = 9.8, which is different from the one with 40 nm PAA membranes (pH = 6.6). The pI of PAA membranes fabricated using different electrolytes varies significantly due to the special adsorption of ions on the alumina surface.[14] For instance, the pI values of PAA membranes fabricated in oxalic acid and phosphoric acid are 6.5 and 5.5 in KCl resolution, respectively.[14] However, the pI of PAA membrane fabricated in sulfuric acid is not yet reported. Recently, we have proven the existence of ion channels in the barrier layer of PAA by electrokinetic experiments.[17] ICR would appear if there is charge on the wall of PAA nanochannels with barrier layer, because the nanochannels size of porous layer and barrier layer is considerably different. ICR experiments were carried out using PAA membrane ended with a barrier layer fabricated in sulfuric acid. As shown in Figure S4 (Supporting Information), the polarity of ICR is reversed between pH = 9.3 and pH = 9.5 due to the rapid change of charge polarity. Thus, the pI of PAA membranes fabricated in sulfuric acid could be estimated as 9.3–9.5.

Until now, there have been no reports on experimental demonstration of the relationship between the rectification behavior and the length of asymmetric surface charge distribution in nanochannels. In this article, the rectification properties of another length nanochannel array (-NH_2 45 μm, -OH 40 μm, fabricated at 50 V in 0.3 M oxalic acid, Supporting Information Figure S5) were investigated. As shown in Supporting Information Figure S6,S7, there is no obvious difference compared with the first nanochannel array (-NH_2 45 μm, -OH 25 μm, fabricated in oxalic acid) (Figure 5A,B, Figure 6A). In the previous report, the depletion zone is about several nanometers to a few tens of nanometers in these nanodevices.[18] If the length of the nanochannels is longer than depletion zone, the ICR ratio would not change obviously. In the present case, the length of nanochannels with asymmetric charge distribution reaches 20–50 μm, which is long enough to form a depletion zone. Thus, the change of charge length has no effect on the ICR ratio. Nevertheless, such PAA membranes with tailorable length of functional layer can be used in other areas, for instance, molecular separation application, targeted drug release and biosensing.

3. Theoretical Simulation

The mechanism of ICR in cylindrical nanochannels with asymmetric surface charge distribution was studied by using the finite element method (FEM) combing with the Poisson-Nernst-Planck (PNP) equation (Equation 5 and Equation 6).

$$\nabla^2\Phi = -\frac{F}{\varepsilon}\sum_i z_i c_i \tag{5}$$

$$J_i = -D_i\nabla c_i - \frac{z_i F}{RT} D_i c_i \nabla\Phi \tag{6}$$

where, J_i, D_i, c_i, z_i and Φ are the ions flux, the diffusion coefficient of species *i*, the concentration of species *i*, the charge of species *i* and the electrical potential, respectively. ε is the dielectric constant of fluid; *F*, *R* and *T* are the Faraday constant, the ideal gas constant and the Kelvin temperature, respectively.

The FEM model was built in the FEM software of COMSOL 3.5a (USA) with 2D axis symmetry along the center axis of nanochannel (Supporting Information Figure S10). To simplify the model, we only simulated single nanochannel by assuming that the nanochannel of PAA has the homogeneous structure and surface characteristics. The origin of the cylindrical coordinate (*r*,*z*) is located at the opening centre of amino modified nanochannel. The boundary conditions in the mathematical model are summarized in Table 1 (Supporting Information), where *Va* is the electric potential varying against the ground potential at boundary h; σ_1 and σ_2 are the surface charge densities on the boundary d and e, respectively. The nanochannel surface with amino group carries minor negative charge (-0.5 mC/m^2) as determined by ionic conductance measurement in the PAA membranes (Supporting Information Figure S11). This may be caused by the formation of a small amount of Si-OH via hydrolysis of a silanization reagent. The surface charge density varies with different solution pH values. In basic solutions, the surface charge density of the segment modified with amino group is not changed, while the one of segment without modification increases quickly as pH increases. Therefore, the surface charge density was set as $\sigma_1 = -0.5$ mC/m^2, $\sigma_2 = -10$ mC/m^2; $\sigma_1 = -0.5$ mC/m^2, $\sigma_2 = -15$ mC/m^2; $\sigma_1 = -0.5$ mC/m^2, $\sigma_1 = -20$ mC/m^2, respectively. In acidic solutions, the surface charge density of the two segments increases simultaneously. However, the surface charge density of unmodified segment is larger than the one of the segment modified with amino group because three Si-O bonded with three Al-OH, generating only one amino ($-NH_2$) group. Thus, the surface charge density was set as σ_1 = 4 mC/m^2, σ_2 = 10 mC/m^2; σ_1 = 6 mC/m^2, σ_2 = 15 mC/m^2; σ_1 = 8 mC/m^2, σ_2 = 20 mC/m^2, respectively. Aqueous solution of 1 mM KCl was used in the computation domain, therefore, the diffusion coefficients of K^+ and Cl^- are set as 1.957×10^{-9} and 2.032×10^{-9} m^2/s. The transport of H^+ and OH^- was not considered in the FEM model, because their concentrations are negligible in the most conditions of our experiments except for

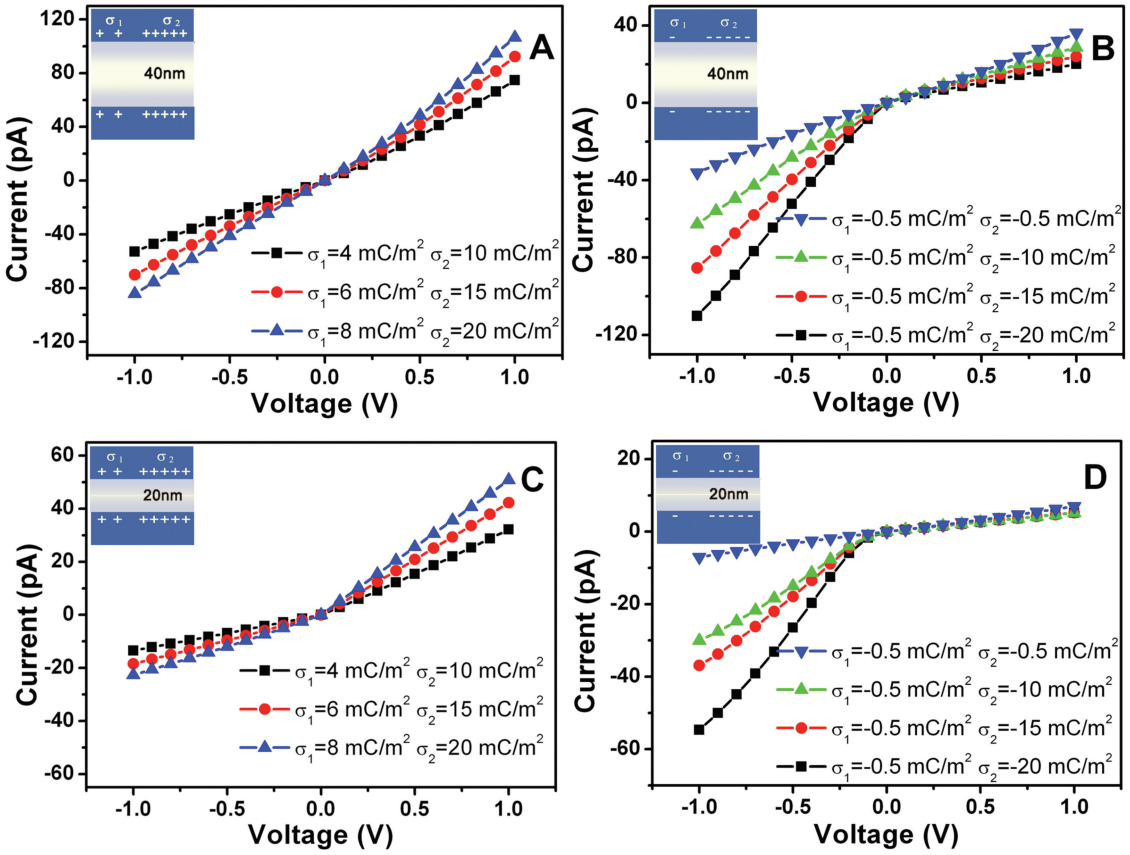

Figure 8. Simulated i-V characteristics of single nanochannels with different diameters (A,B: 40 nm; C,D: 20 nm;) and the different surface charge densities. A,C) nanochannel surface with positive charge in low pH solutions. B,D) nanochannel surface with negative charge in high pH solutions). σ_1 and σ_2 represent the surface charge densities of the different surface in nanochannel.

pH = 3.0 and pH = 11.0 solutions. In addition, the transport modes of H^+ and OH^- are entirely different from other ions (K^+, Na^+, Cl^-, SO_4^{2-}, et al.) in nanochannels. The whole simulated results are achieved based on *Va* from −1 to +1 V for the 20 and 40 nm nanochannels. The resulting ionic current was obtained by integrating the ionic flux on the boundary h or a. (Equation 7)

$$I = -F \int_s \left(J\left(K^+\right) - J\left(Cl^-\right)\right) n ds \tag{7}$$

The i-V characteristics of single nanochannel were simulated at varied voltage bias ranging form -1 to +1V. As illustrated in **Figure 8**, the rectification ratios of 20 nm channel (Figure 8C,D) are larger than 40 nm channel (Figure 8A,B). These can be attributed to ionic flux variation in nanochannel induced by static electric potential and electric migration. The detailed discussion is presented in the next section. It is clear that for acidic conditions, the whole rectification ratios are smaller than in the alkaline conditions. The rectification ratio for the 20 nm nanochannel ranges from 2.24 to 2.38 (Figure 8C); while the one for 40 nm nanochannel ranges from 1.26 to 1.41 (Figure 8A). Since the protonated amino groups ($-NH_3^+$) and unmodified protonated alumina ($-OH_2^+$) are positively charged in acidic conditions (insets in Figure 8A,C), lower asymmetric surface charge distribution along the nanochannel results in lower rectification ratio. When the nanochannel in alkaline conditions, the intrinsic alumina is deprotonated and carries negatively charges at high pH values, while the amino group is neutral. This would induce higher asymmetry in the profile of surface charge density (insets in Figure 8B,D).

Although single nanochannel model is used in the FEM simulation, the theoretically simulated results are in reasonable agreement with the experimental data. The discrepancies between the theory and experiments are partly due to the uncertain factors since many factors were not included in the model. First, the transport of proton and hydroxyl ions is not considered. Second, possible cross interference of neighboring nanochannels on the ion transport is not considered in the single nanochannel model. Third, there is more or less with a degree of difference about the surface charge density between the theory and experiments.

To explain qualitatively the ICR effect appeared in the selected modified nanochannel, the concentration profiles of K^+ and Cl^- through the nanochannel carrying negative and positive charges at ±1 V bias were analyzed. First, we discussed the ion profiles in a nanochannel carrying negative charges. As illustrated in Supporting Inforamtion Figure S12A,C, there is

obvious depletion of K^+ and Cl^- concentrations in the nanochannel as +1 V bias was added, especially in the unmodified nanochannel. However, the reversed bias (-1 V) produces high ionic concentration in the corresponding region, leading to the formation of an enrichment zone (Supporting Information Figure S12B,D). Therefore, the formation of the ion depletion and enrichment zones in nanochannel results in ionic current variation at close state (+1 V) and open state (-1 V). The corresponding variation of electric potential refers to the Supporting Information (Figure S14). When the diameter of nanochannel is reduced to 20 nm, the ion depletion and enrichment effects are more pronounced than the 40 nm channel. Thus higher rectification ratio can be obtained in the 20 nm nanochannel.

Under low pH conditions, both the protonated amino groups ($-NH_3^+$) and unmodified protonated alumina ($-OH_2^+$) are positively charged. However, the difference in the positive surface charge density in acidic solutions is smaller than the one in alkaline solutions. Therefore, the low rectification ratio can be attributed to the weaker ion depletion and enrichment regions in the channel with positive charge. As illustrated in Supporting Information Figure S13 for the 40 nm nanochannel, the depletion zone (Supporting Information Figure S13B) is narrower in acidic solutions than in alkaline solutions (Supporting Information Figure S12A). For the 20 nm diameter channel, the width of the depletion zone (Supporting Information Figure S13D) in acidic solutions is comparable to the one in alkaline solutions (Supporting Information Figure 12C). However, the total ion concentration in acidic solutions is higher than the one in alkaline solutions. These phenomena can be also observed in Supporting Information Figure S13B,S12A. When the direction of voltage bias is changed, the enrichment zone and the open state are formed in the nanochannel (Supporting Information Figure S13A,C). However, compared with the results in Supporting Information Figure S12B,D, the ion enrichment concentration in acidic solutions is considerable lower than in alkaline solutions. Thus, the weaker ion depletion and enrichment zones induced by lower asymmetric surface charge distribution result in smaller rectification ratio.

4. Conclusions

In conclusion, we demonstrate that pH-dependent ionic current rectification can be achieved by APTMS function at designed positions in PAA membranes. The asymmetric charges distribution arising from selective modification along the nanochannel axis dominates the ICR effect. Thus, the isoelectric point of nanochannels can be easily estimated to be the value with unit rectification ratio. In addition, the diameter of the nanochannels plays a more important role than modification length in ICR. The results demonstrate that the rectification polarity and rectification ratio required in practical applications can be accomplished with the same device by simply varying solution pH values, which closely mimic the gating mechanism of biological channels. FEM simulation shows that the surface charge plays a dominating role in transport of ions when the size of nanochannels is comparable to the thickness of the electrical double layer. The high conductance state can be attributed to ions accumulation within the nanochannels. On the contrary, ions depletion results in low conductance state. We believe that such simple and economically affordable nanochannel array would be applicable in areas such as biosensing, molecular transport and separation, and drug delivery in confined environments.

5. Experimental Section

Chemicals and Reagents: The aluminum sheets (thickness 0.1 mm; purity 99.99%) were obtained from Xinjiang Zhonghe Limited Corp. (Xinjiang, China). Analytical grade reagents of oxalic acid, sulfuric acid, phosphoric acid, perchloric acid, 36% hydrochloric acid aqueous solution, potassium hydroxide, potassium chloride, stannous chloride, ethanol, acetone, and 30% hydrogen peroxide aqueous solution were purchased from Sinopharm Chemical Reagent Co., Ltd.. 3-aminopropyltrimethoxysilane was from Sigma-Aldrich. All solutions were prepared daily with deionized water (18.2 MΩ cm^{-1}, Milli Q). Prior to use, the KCl solutions were all passed through a 0.22 μm filter.

Fluorescence Labeling: Fluorescence labeling was performed by treating the membranes with 20 μg/mL of fluorescein isothiocyanate (FITC) in 100 mM phosphate buffered saline (PBS) buffer (pH 7.2) at room temperature for 12 h. The unbounded dye was washed off by rinsing with large amount of PBS buffer.

Characterizations: Scanning electron microscopy (SEM) images were acquired on a scanning electron microscope (S-4800 Hitachi, Japan) with a 8 mm working distance and 10 kV accelerating voltage. Laser scanning confocal microscopy (LSCM) images of double-layered PAA membranes labeled with FITC were obtained on a laser scanning confocal microscope (TCS SP5 C1-Z, Leica, Germany). Excitation wavelength was 488 nm, and emission wavelength was 510–530 nm. X-ray photoelectron spectroscopy (XPS) of PAA membranes without (bare PAA) and with APTMS modification were measured using a X-ray photoelectron spectroscopy (K-Alpha, Thermo Fisher Scientific, America).

Measurement Setup and i-V Characterizations: Supporting Information Figure S1 shows the scheme of ionic current measurement device featuring nanochannel array bridged two electrolytic cells. The effective exposure area of nanochannel array was 3.14 mm^2 in the present study. The membrane was clamped between two PDMS films and then placed between two Teflon cells. All ionic current measurements were carried out in the same conductivity bath in a home-made Faraday shielding cage, which has the same ground with all other instruments used. Two Ag/AgCl electrodes were used for applying the trans-membrane potential and measuring the ionic current, since Ag/AgCl electrodes are nonpolarizable and very stable. Linear sweep voltammetry was carried out on a CHI 1140 electrochemical workstation (CHI Instrument Co. Ltd., USA). The ionic currents through the nanochannel array were measured by scanning the voltage from −1 V to +1 V at a scan rate of 100 mV/s. The pure KCl solution was slightly acidic (pH 6.6) under the conditions due to the dissolution of CO_2 from atmosphere. The solution pH could be adjusted with either 0.1 M HCl or 0.1 M KOH.

Mass-Transport Experiment: The experimental setup is similar to the ionic current measurement device, as shown in Figure S1 in the Supporting Information. Prior to measurements, the membranes were left for at least 1 h in 1mM KCl solution to ensure complete wetting. Mass-transport experiments were carried out by adding 2.0 mL of 1 mM KCl solution containing 1mM $Ru(bpy)_3Cl_2$ to the feed half-cell and 1mM KCl solution to the permeation half-cell. The solution pH was adjusted by either 0.1 M HCl or 0.1 M KOH. The diffusion flux was determined by monitoring the concentration change of $Ru(bpy)_3Cl_2$ in the permeation half-cell. This was accomplished by fluorescence detection of the permeation solution with a fluorescence spectrophotometer (Varian Cary Eclipse, USA) at 610 nm. The excitation wavelength was 488 nm. The absorbance data were converted to moles of $Ru(bpy)_3Cl_2$ transported with the aid of a calibration curve (Supporting Information Figure S9).

Supporting Information

Supporting Information is available from the Wiley Online Library or from the author.

Acknowledgements

This work was supported by the grants from the National 973 Basic Research Program (2012CB933800), the National Natural Science Foundation of China (21035002, 21121091), the Ministry of Education of China (200802840012), the Natural Science Foundation of Jiangsu Province (BK2010009) and Innovation Project for College Graduates of Jiangsu Province (CXZZ11_0029). The authors also gratefully acknowledge the HPCC (High-Performance Computing Center) of Nanjing University.

Received: January 26, 2013
Published online: April 4, 2013

[1] a) R. B. Schoch, J. Han, P. Renaud, *Rev. Mod. Phys.* **2008**, *80*, 839; b) W. Sparreboom, A. van den Berg, J. C. T. Eijkel, *Nat. Nanotechnol.* **2009**, *4*, 713; c) Z. S. Siwy, S. Howorka, *Chem. Soc. Rev.* **2010**, *39*, 1115; d) X. Hou, W. Guo, L. Jiang, *Chem. Soc. Rev.* **2011**, *40*, 2385; e) C. Wang, J. Xu, H. Chen, X. Xia, *Sci. Chin. Chem.* **2012**, *55*, 453.

[2] G. Hummer, J. C. Rasaiah, J. P. Noworyta, *Nature* **2001**, *414*, 188.

[3] a) M. Majumder, N. Chopra, R. Andrews, B. Hinds, *Nature* **2005**, *438*, 930; b) H. Chinen, K. Mawatari, Y. Pihosh, K. Morikawa, Y. Kazoe, T. Tsukahara, T. Kitamori, *Angew. Chem. Int. Ed.* **2012**, *51*, 3573.

[4] a) K. B. Jirage, J. C. Hulteen, C. R. Martin, *Science* **1997**, *278*, 655; b) C. C. Striemer, T. R. Gaborski, J. L. McGrath, P. M. Fauchet, *Nature* **2007**, *445*, 749; c) E. N. Savariar, K. Krishnamoorthy, S. Thayumanavan, *Nat. Nanotechnol.* **2008**, *3*, 112; d) M. Ali, S. Nasir, Q. H. Nguyen, J. K. Sahoo, M. N. Tahir, W. Tremel, W. Ensinger, *J. Am. Chem. Soc.* **2011**, *133*, 17307; e) T. Komatsu, X. Qu, H. Ihara, M. Fujihara, H. Azuma, H. Ikeda, *J. Am. Chem. Soc.* **2011**, *133*, 3246; f) R. Wei, V. Gatterdam, R. Wieneke, R. Tampe, U. Rant, *Nat. Nanotechnol.* **2012**, *7*, 257.

[5] a) J. C. Hulteen, K. B. Jirage, C. R. Martin, *J. Am. Chem. Soc.* **1998**, *120*, 6603; b) C. R. Martin, M. Nishizawa, K. Jirage, M. Kang, S. B. Lee, *Adv. Mater.* **2001**, *13*, 1351; c) C. Wei, A. J. Bard, S. W. Feldberg, *Anal. Chem.* **1997**, *69*, 4627; d) Z. Siwy, E. Heins, C. C. Harrell, P. Kohli, C. R. Martin, *J. Am. Chem. Soc.* **2004**, *126*, 10850; e) S. Umehara, N. Pourmand, C. D. Webb, R. W. Davis, K. Yasuda, M. Karhanek, *Nano Lett.* **2006**, *6*, 2486; f) I. Vlassiouk, Z. S. Siwy, *Nano Lett.* **2007**, *7*, 552; g) M. Ali, P. Ramirez, S. Mafé, R. Neumann, W. Ensinger, *ACS Nano* **2009**, *3*, 603; h) B. Yameen, M. Ali, R. Neumann, W. Ensinger, W. Knoll, O. Azzaroni, *J. Am. Chem. Soc.* **2009**, *131*, 2070; i) S. J. Li, J. Li, K. Wang, C. Wang, J. J. Xu, H. Y. Chen, X. H. Xia, Q. Huo, *ACS Nano* **2010**, *4*, 6417; j) W. J. Lan, D. A. Holden, H. S. White, *J. Am. Chem. Soc.* **2011**, *133*, 13300; k) D. Momotenko, H. H. Girault, *J. Am. Chem. Soc.* **2011**, *133*, 14496; l) M. Zhang, X. Hou, J. Wang, Y. Tian, X. Fan, J. Zhai, L. Jiang, *Adv. Mater.* **2012**, *24*, 2424; m) S. W. Kowalczyk, L. Kapinos, T. R. Blosser, T. Magalhaes, P. van Nies, Y. H. LimRoderick, C. Dekker, *Nat. Nanotechnol.* **2011**, *6*, 433; n) B. M. Venkatesan, R. Bashir, *Nat. Nanotechnol.* **2011**, *6*, 615; o) H. L. Gao, C. Y. Li, F. X. Ma, K. Wang, J. J. Xu, H. Y. Chen, X. H. Xia, *Phys. Chem. Chem. Phys.* **2012**, *14*, 9460.

[6] a) R. Karnik, C. Duan, K. Castelino, H. Daiguji, A. Majumdar, *Nano Lett.* **2007**, *7*, 547; b) I. Vlassiouk, T. R. Kozel, Z. S. Siwy, *J. Am. Chem. Soc.* **2009**, *131*, 8211; c) J. Liu, M. Kvetny, J. Feng, D. Wang, B. Wu, W. Brown, G. Wang, *Langmuir* **2011**, *28*, 1588; d) L. X. Zhang, S. L. Cai, Y. B. Zheng, X. H. Cao, Y. Q. Li, *Adv. Funct. Mater.* **2011**, *21*, 2103; e) M. Ali, P. Ramirez, H. Q. Nguyen, S. Nasir, J. Cervera, S. Mafe, W. Ensinger, *ACS Nano* **2012**, *6*, 3631; f) M. Ali, B. Yameen, J. Cervera, P. Ramírez, R. Neumann, W. Ensinger, W. Knoll, O. Azzaroni, *J. Am. Chem. Soc.* **2010**, *132*, 8338; g) L. J. Cheng, L. J. Guo, *ACS Nano* **2009**, *3*, 575; h) S. M. Wu, F. Wildhaber, O. Vazquez-Mena, A. Bertsch, J. Brugger, P. Renaud, *Nanoscale* **2012**, *4*, 5718.

[7] a) E. A. Heins, L. A. Baker, Z. S. Siwy, M. O. Mota, C. R. Martin, *J. Phys. Chem. B* **2005**, *109*, 18400; b) M. L. Kovarik, K. Zhou, S. C. Jacobson, *J. Phys. Chem. B* **2009**, *113*, 15960; c) M. Ali, Q. H. Nguyen, R. Neumann, W. Ensinger, *Chem. Commun.* **2010**, *46*, 6690; d) L. X. Zhang, X. H. Cao, Y. B. Zheng, Y. Q. Li, *Electrochem. Commun.* **2010**, *12*, 1249; e) M. Ali, M. N. Tahir, Z. Siwy, R. Neumann, W. Tremel, W. Ensinger, *Anal. Chem.* **2011**, *83*, 1673; f) S. Liu, Y. Dong, W. Zhao, X. Xie, T. Ji, X. Yin, Y. Liu, Z. Liang, D. Momotenko, D. Liang, H. H. Girault, Y. Shao, *Anal. Chem.* **2012**, *84*, 5565.

[8] R. Yan, W. Liang, R. Fan, P. Yang, *Nano Lett.* **2009**, *9*, 3820.

[9] R. Karnik, K. Castelino, C. Duan, A. Majumdar, *Nano Lett.* **2006**, *6*, 1735.

[10] a) W. Chen, Z. Q. Wu, X. H. Xia, J. J. Xu, H. Y. Chen, *Angew. Chem. Int. Ed.* **2010**, *49*, 7943; b) C. Duan, A. Majumdar, *Nat. Nanotechnol.* **2010**, *5*, 848.

[11] A. M. M. Jani, I. M. Kempson, D. Losic, N. H. Voelcker, *Angew. Chem. Int. Ed.* **2010**, *49*, 7933.

[12] a) A. P. Li, F. Muller, A. Birner, K. Nielsch, U. Gosele, *J. Appl. Phys.* **1998**, *84*, 6023; b) W. Chen, J. S. Wu, X. H. Xia, *ACS Nano* **2008**, *2*, 959; c) W. Lee, R. Ji, U. Gosele, K. Nielsch, *Nat. Mater.* **2006**, *5*, 741; d) J. H. Yuan, F. Y. He, D. C. Sun, X. H. Xia, *Chem. Mater.* **2004**, *16*, 1841.

[13] a) H. Miedema, M. Vrouenraets, J. Wierenga, W. Meijberg, G. Robillard, B. Eisenberg, *Nano Lett.* **2007**, *7*, 2886; b) H. Y. Wang, Y. L. Ying, Y. Li, H. B. Kraatz, Y. T. Long, *Anal. Chem.* **2011**, *83*, 1746.

[14] W. Chen, J. H. Yuan, X. H. Xia, *Anal. Chem.* **2005**, *77*, 8102.

[15] H. L. Gao, K. L. Zhou, C. Wang, S. J. Li, H. Zhang, X. H. Xia, *J Electrochem.* **2012**, *18*, 229.

[16] H. Masuda, F. Hasegwa, S. Ono, *J. Electrochem. Soc.* **1997**, *144*, L127.

[17] W. Chen, B. Jin, Y. L. Hu, Y. Lu, X. H. Xia, *Small* **2012**, *8*, 1001.

[18] I. Vlassiouk, S. Smirnov, Z. Siwy, *ACS Nano* **2008**, *2*, 1589.